Video-rate Dual-modal Wide-beam Harmonic Ultrasound and Photoacoustic Computed Tomography

Yachao Zhang[1,2,3], Yue Wang[1,2], Puxiang Lai[3], Lidai Wang[1,2]*

[1]City University of Hong Kong, Department of Biomedical Engineering, Kowloon, Hong Kong SAR, China

[2]City University of Hong Kong, Shenzhen Research Institute, Shenzhen, China

[3]Department of Biomedical Engineering, Hong Kong Polytechnic University, Hong Kong, China.

Abstract: Dual-modal ultrasound (US) and photoacoustic (PA) imaging have tremendous advantages in biomedical applications, such as pharmacokinetics, cancer screening, and imaging-guided surgery. Compared with ring-shaped arrays, a linear piezoelectric transducer array is applicable to more anatomical sites and has been widely used in US/PA imaging. However, the linear array may limit the imaging quality due to narrow bandwidth, partial detection angle, or inadequate spatial sampling rate. To meet clinic demand of high-quality US/PA imaging without complicating the linear transducer hardware, we develop a video-rate wide-beam harmonic ultrasound (WBHUS) and single-shot PA computed tomography. The harmonic US imaging employs pulse phase inversion to reduce clutters and improve spatial resolution. Wide-beam US transmission can shorten the scanning times by 267% and enables a 20-Hz dual-model imaging rate, which minimizes motion artifacts *in vivo* imaging. The harmonic US imaging does not only provide accurate anatomical references for locating PA features, but also reduces some artifacts in PA images. The improved image quality allows us to acquire high-resolution anatomical structures in deep tissue without labeling. The fast imaging speed enables visualizing interventional procedures and monitoring the pulsations of the thoracic aorta and radial artery in real-time. The video-rate dual-modal harmonic US and single-shot PA computed tomography usea clinical-grade linear-array transducer and thus can be readily implemented in clinical US imaging.

Index Terms—Harmonic ultrasound imaging; high-speed imaging; linear-array ultrasound transducer; photoacoustic imaging; wide-beam transmission;

1. Introduction

Ultrasound (US) imaging is widely used to distinguish morphological features based on acoustic impedance mismatch [1]. Photoacoustic (PA) tomography can image chromophores with high spatiotemporal resolution at several-centimeters depths [2][3][4][5][6]. Integrated dual-modal US/PA imaging can provide complementary contrasts for diagnosis and surgical guidance. Both US and PA imaging involve reconstruction from acoustic signals and thus can be readily integrated into one system. Therefore, simultaneous dual-modal US and PA imaging has been recognized as a promising tool for many clinical and preclinical applications, such as early cancer diagnosis, assessing nanomedicine in tumor therapy [7][8][9][10], and imaging-guided surgery [11][12][13].

Various US/PA imaging systems using different types of transducers have been explored. The detection transducers can be categorized into spherical single-element transducer[14][15], linear-array transducer[16][17][18][19][20], arc-shape transducer[21][22][23][24], spherical 3D-matrix transducer array[25], and the linear-concave hybrid transducer[26]. Most of them are optimized for small animal imaging, instead of human imaging. For example, a ring-shaped or hybrid multi-segment transducer with high-density elements ($\geq$256) can obtain high-quality PA images via alleviating the limited view and providing adequate spatial sampling rate but has several limitations in clinical applications. Firstly, the transducer is designed for pre-clinical research and is not suitable for human imaging. Secondly, because the transducer is customized, and existing clinical-grade US transducer cannot be fully utilized, dual-modal imaging will increase the cost. Thirdly, the large element number increases the burden on data acquisition, transfer, storage, and processing, especially for high-speed dual-modal imaging. A high-resolution dual-modal US/PA imaging system compatible with clinical low-frequency linear-array transducers has not been thoroughly investigated.

A clinical linear-array transducer usually has a 2-8-MHz central frequency. With such a low-frequency linear transducer, PA imaging may suffer from limited view, degraded

resolution, or out-of-focus artifacts. Thus, co-registered high-resolution US images are of great importance to locate the PA features. Compared with conventional US imaging, harmonic US imaging offers higher resolution and can be more suitable for identifying the PA features. To date, the fusion of PA and harmonic US imaging on a clinical-grade linear-array transducer has not been investigated.

Here, we report a dual-mode imaging platform that integrates wide-beam harmonic ultrasonography (WBHUS) and PA computed tomography at a video rate. The system uses a clinical-grade linear-array transducer for animal and human imaging. The harmonic US imaging does not only provide a high-resolution anatomical reference for the PA features, but also enhances PA imaging quality via artifacts removal. To achieve high imaging speed, a collaborative scheme of wide beam transmission and pulse phase inversion is implemented to shorten the scanning times. The system features a high spatial resolution of co-registered US/PA tomographic imaging and single-breath-hold 3D imaging ability. We successfully demonstrate the system on dual-contrast anatomical imaging, visualizing interventional procedures of dye injection, and monitoring of hemodynamics in animal and human.

2. Materials and methods

Definitions

Three directions are defined and unified for the linear-array imaging system. The axial direction (z) refers to the direction parallel to the acoustic beam axis, and the lateral direction (x) is perpendicular to the acoustic beam axis in the imaging plane. The elevational direction (y, slice thickness) is orthogonal to the imaging plane. The 3D scanning is in line with the elevational direction.

Experiment setup

The hardware and software of the WBHUS/PA imaging platform are schematically depicted in Fig. 1 and Supplementary Fig. S1. The hardware comprises an illumination source for PA excitation, a handheld 3D scanner, and a data acquisition (DAQ) system.

The illumination source is an optical parametric oscillator (OPO) pumped by an Nd: YAG pulsed laser (Spectra-Physics, Santa Clara, CA, USA). The source offers 5-8-ns pulse width and 20-Hz pulse repetition frequency (PRF). The wavelength is tunable between 410 and 2500 nm. The laser beam is coupled into a customized 1×2 optical fiber bundle with an input diameter of 11.7 mm. The other end of the fiber bundle are two rectangular surfaces (35 mm×1 mm each, Fig. 1d) and mounted on two sides of a linear transducer. The linear-array transducer has 128 elements, 6.25-MHz central frequency, 0.3-mm pitch, and 20-mm elevation focus and is used for both US and PA imaging. The US/PA probe, including the transducer and the fiber bundle, is mounted on a 3-axis translation stage. The DAQ system (Vantage US research system from Verasonics Inc.) can transmit US signals and digitize US and PA signals. The sampling rate is 50 MHz, and the analog-to-digital (A/D) conversion resolution is 14 bit. The laser, DAQ, and translation stage are synchronized by a microcontroller (Mega 2560, Arduino) for laser-firing, US/PA imaging, and motion control.

The software includes a synchronization module and a US/PA reconstruction module (see Fig. 1b and Supplementary Fig. S1). The synchronization module provides handshake signals between the DAQ and the laser so that the US and PA images can be accurately co-registered. The details can be seen in Supplementary Fig. S2a. Firstly, the laser lamp operates at 20 Hz and sends a TTL trigger signal to the DAQ. After delaying by 200 μs, the DAQ sends a signal to trigger the laser Q-switch. However, there is still a short delay (1-1.5 μs) between the laser firing and PA signal acquisition. The DAQ initialization may cause misalignment between the US and PA images. We use a calibration method to correct the misalignment without extra hardware synchronization. Weak light is deflected to the transducer surface to excite a PA signal. Then we record the peak position of the PA signal from the transducer surface (Supplementary Fig. S2b), which can correct the jitter between the laser firing and the PA acquisition.

Wide-beam harmonic US and single-shot PA imaging

To acquire harmonic US signals, at each step, the transducer transmits two successive acoustic beams with identical pulse numbers but opposite polarities. To increase the

imaging speed, partial transducer elements are grouped to transmit a wide beam, and all transducer elements are used for receiving. To scan the entire field of view, the indexes of the transmission elements are sequentially changed along the lateral direction. The details of the transmission map can be found in Fig.2a and Supplementary Fig. S3. The total scanning steps for the WBHUS is 96.

In Supplementary Fig. S5a and S5b, we compare the US transmission map with focused imaging (FI) and plane-wave (PW) imaging. In FI, the focal depth of the transmitted beam is equal to the elevational focus. In PW, the focal depth of the transmitted beam is set to infinite. In comparison, WBHUS sets the transmitted focal depth to five times of the elevational focus and covers a wider area than FI. Thus, WBHUS takes less scanning time than FI.

For PA imaging, all elements receive the signal after each laser shot. The sampling rate is 50 MHz for both US and PA signals. After A/D conversion, the US and PA signals are first filtered with a 25-MHz lowpass filter for antialising purpose and then processed with two different bandpass filters seperately. For the US signal, the bandpass filter is designed to suppress the fundamental frequency and pass the harmonic signals. Because the US transmission frequency is 5.95 MHz, the BPF has a 3-dB bandwidth from 6.25 to 18.75 MHz and a 6-dB bandwidth from 4.59 to 20.41 MHz. For the PA signal, to improve the signal-to-noise ratio, the bandpass filter has a 3-dB bandwidth of 3.5-10.25 MHz and a 6-dB bandwidth of 2.12-11.76 MHz. In addition, the PA data in each channel are filtered with a 2nd order Butterworth bandpass filter (0.1 MHz - 10 MHz).

Image reconstruction and enhancement

We use the coherent delay-and-sum (DAS) algorithm for US and PA reconstruction [22]. Both US and PA reconstruction adopt directivity weighting compensation ($w_{\theta k}$) to mitigate image artifacts. The compensation formula is written as,

$$\begin{aligned} w_{\theta k} &= A\left(\cos(\theta_i)\frac{\sin(\hat{X})}{\hat{X}}\right) \\ \hat{X} &= \frac{width}{c/f}\pi sin(\theta_i) \end{aligned}, \quad (1)$$

where A represents the absolute value function. The θ_i is the angle of the PA wave with respect to the normal direction of the k^{th} element, $width$ is the width of the

transducer element, f is the central frequency of the transducer, and c is the sound speed. Here, $cos(\theta_k)$ accounts for the directional sensitivity and $\frac{\sin(\hat{X})}{\hat{X}}$ compensates for the detection sensitivity related to the transducer element size and the central frequency. To increase the image contrast, a fractional power is applied to the reconstructed US and PA images. After DAS, the envelopes of US and PA images are detected along the axial direction.

The US/PA frame rate is 20 Hz and is mainly limited by the laser PRF. This is fast enough for most hemodynamic monitoring for animals and humans.

We develop a US-assisted method for PA image enhancement. Because of the melanin absorption in the epidermis and optical attenuation in tissue, the PA signals from the skin are much stronger than those from the deep tissue. To better visualize deep features, we segment the skin signals from others in the co-registered US/PA images [27][28]. The segmentation curve is a quintic polynomial. The epidermal boundary in the US image determines the slope of the segmentation curve. The PA signal of the epidermis offers the axial position. The PA image is divided into two parts according to the segmentation curve. In the maximum amplitude projection (MAP) and the 3D PA images, we plot only the signals underneath the segmented skin layer to show the deep vascular features.

To improve PA contrast and suppress noises, we use a two-step approach to enhance the vessel features[29]. Firstly, we use a modified Hessian-based Frangi vesselness filter to process the PA MAP images. The filter applies different scales between 1 and 80 pixels with a step of 5 pixels. Then a contrast-limited adaptive histogram equalization (CLAHE) algorithm is applied at each scale [30][31], and the sub-images are averaged to reconstruct the enhanced image. For the 3D data, we use a 3D median filter with a kernel size of three on each dimension to suppress noises and jitters. All data processing was implemented in MATLAB (2019b, MathWorks, USA) on a computer (Inter Core i7@2.60 GHz, 16 GB of RAM, NVIDIA GeForce RTX 2060).

System characterization

We characterized the spatial resolution, signal-to-noise ratio (SNR), and contrast-to-noise ratio (CNR) of the dual-model system. A tungsten wire with a 20-μm diameter was used to measure the spatial resolution of US and PA imaging in deionized water. The optical wavelength for PA imaging is 532 nm. The SNR and CNR at different positions are compared between WBHUS and FI harmonic US (FIHUS) via imaging an adult index finger joint at the distal interphalangeal (DIP). The FIHUS is a combination of focused imaging and second-harmonic US imaging. The cross-sections of the blood vessels in the US images show a hypoechoic region. The SNR and CNR are calculated from the following equations,

$$SNR = 20log_{10}(\frac{\bar{I}_{signal}}{\sigma_{background}}), \quad (2)$$

$$CNR = 20log_{10}(\frac{abs(\bar{I}_{signal}-\bar{I}_{background})}{\sqrt{\sigma_{signal}^2+\sigma_{background}^2}}), \quad (3)$$

where $\bar{I}_{signal}$ is the average intensity in the selected blood vessel region, $\bar{I}_{background}$ is the average intensity of the selected background region, σ_{signal} and $\sigma_{background}$ are the standard deviations of the blood vessel signals and the background noises.

To further demonstrate the resolution of WBHUS in deep tissue, we imaged a pencil lead (2-mm diameter) at 17-mm depth in fresh chicken breast tissue. The resolution is compared with focused imaging and plane-wave imaging.

Imaging-guided interventional procedures in vitro

Taking advantage of high imaging speed and US/PA dual-modal imaging ability, we imaged the dynamic process of indocyanine green (ICG) injection in chicken breast tissue. The ICG is excited with an 808-nm wavelength for PA imaging (8.6 mJ/cm^2). Enabled by the video-rate dual-model imaging speed, we can track the tissue, the needle, and the ICG in real-time. Firstly, the needle (25 G) was inserted into the chicken breast. At a designated position, the ICG solution was first injected at a slow speed and then finished with a high injection speed.

Small animal imaging

Healthy nude mice (9 weeks old, 27g - 30g) were used for in vivo US/PA imaging. The mice were anesthetized with 1.2% (v/v) vaporized isoflurane and placed on a heating pad (37 °C) in a supine position. A membrane-sealed water tank was placed on top of the abdomen. US gel was applied between the abdomen and the membrane for ultrasonic coupling. The US/PA probe was scanned in the elevational direction for 3D imaging. The scanning range was 42 mm, covering from the liver to the heart. The scanning speed was 5 mm/s. The step size was 0.5 mm. To optimize PA excitation of the liver, we compared different wavelengths in the visible and near-infrared spectrum (Supplementary Fig. S8a). The result shows that the 1064-nm wavelength offers the best PA liver or thoracic aorta imaging because of high pulse energy, reduced scattering, and relatively low background absorption. The fluence on the skin was 13.2 mJ/cm^2 and was within the ANSI safety limit of 100 mJ/cm^2 [32]. All animal procedures have been approved by the animal ethical committee of the City University of Hong Kong.

Hemodynamics of the thoracic aorta

With real-time US/PA imaging, we visualized the hemodynamics of the thoracic aorta. We acquired 10-seconds cross-section images of the heart. A region of interest (Line R2 in Fig. 4a) is selected from the co-registered US and PA images. The harmonic US image provides a high-resolution anatomical reference for the thoracic aorta. The dynamics of the aorta are analyzed by calculating the displacement and the total hemoglobin concentration changes induced by heart beating. The wavelength for PA imaging was 1064 nm. The laser fluence on the skin surface was ~13.2 mJ/cm^2.

To calculate the displacement change, the PA profiles centered at the thoracic aorta (labeled as a white solid line in Fig. 4d) with 36-pixel width are extracted. The PA profiles at different times are plotted. The time trace of the aorta (blue solid line in Fig. 4f) is calculated via averaging the amplitude in the displacement direction. We can observe the aorta pulsation frequency in the temporal spectrum.

To analyze the total hemoglobin concentration changes over time, we segment the pulsated thoracic aorta from the background with a two-step method. In the first step, a circle region with an 18-pixels radius is selected around the aorta to segment the images.

The circle region covers the full range of the aorta motion. The barycenter of the circle region is calculated to determine the center coordinates with sub-pixel resolution. In the second step, an 8-pixels-radius circle region around the calculated center coordinates is selected for fine segmentation. The average intensity (Fig. 4h) in this small circle region is calculated as the PA signal of the aorta.

In the spectral analysis of displacement and amplitude changes, the acquired time-trace signals are firstly filtered with a second-order high-pass filter (0.5 Hz) to remove low-frequency interferences. Then a zero-phase digital filter is applied to avoid phase change.

Human imaging

A healthy adult volunteer was recruited for imaging. All experiment procedures and cautions were explained to the volunteer before experiments. During imaging, the volunteer wore safety goggles and fixed their index finger or forearm on an adjustable stage. US gel was applied to the skin to avoid air gap between the skin and the probe. We conducted elevational scanning (5 mm/s) over 50 mm for finger imaging and over 60 mm for forearm imaging. The scanning step size was 0.5 mm. Different wavelengths were compared for optimal PA imaging of the finger and the forearm (Supplementary Fig. S8a). 1064 nm was selected for deep vascular imaging. The fluence on the skin surface was about 13.2 mJ/cm^2. All human experimental procedures have been carried out in conformity with the research committee of the City University of Hong Kong.

Hemodynamics of human radial artery

To monitor the human radial artery pulsation, we first determine the arterial position in the co-registered US/PA images (Line R1 in Fig. 6a). The fluence on the skin surface was about 18.4 mJ/cm^2 (1064 nm) and was within the ANSI safety limit. We first extract the time trace of the artery (A1 in Fig. 6b) from the video-rate US/PA images. The method to compute the displacement is the same as the one for the animal thoracic aorta, except that a 15-pixel radius for fine segmentation was used here.

We use the heart-beat frequency to encode the PA images so that we can enhance the

contrast of the arteries. Firstly, temporal spectral analysis is applied to the time trace of the radial artery signal. The peak frequency is determined as the heart-beat frequency. Then Fourier transformation is applied to every pixel of the PA image. The magnitude of the heart-beat frequency is used to encode the pseudo color of each pixel. Using this method, more arteries become visible.

3. Results

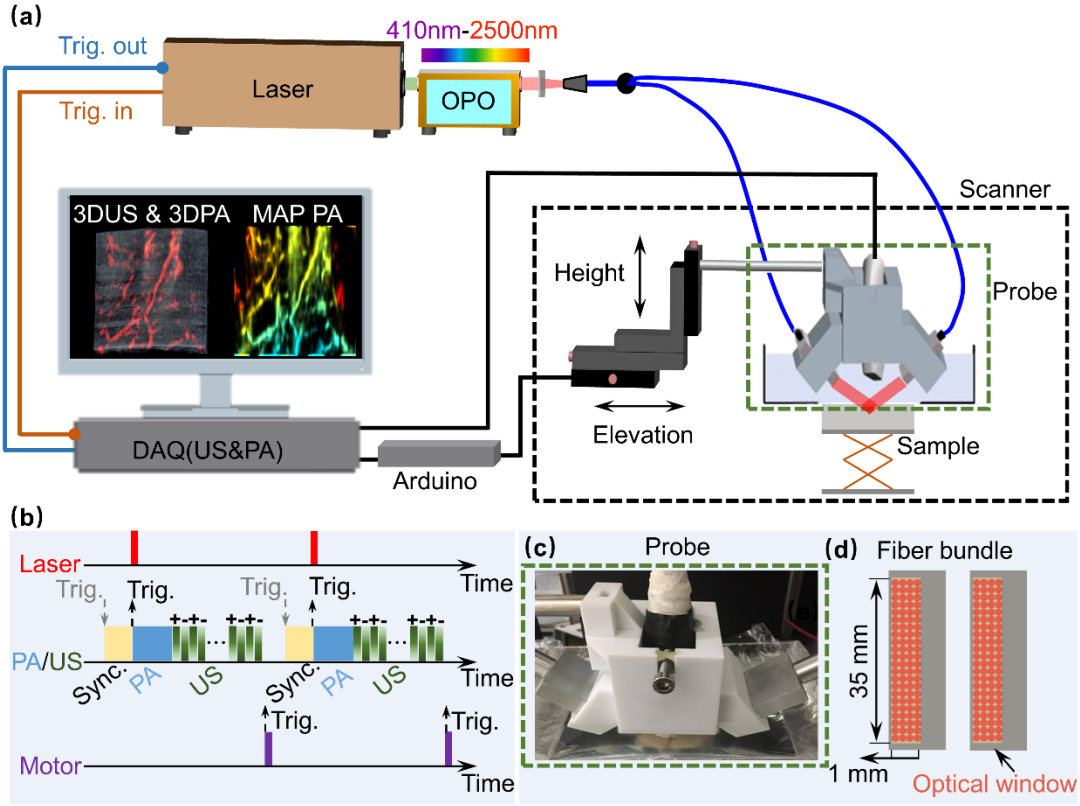

Fig. 1. Video-rate WBHUS/PA dual-modal imaging platform. **(a)** Schematic of the imaging system. **(b)** Time sequence for laser trigger, US/PA transmission/acquisition, and motion control. **(c)** Photography of the integrated handhold US/PA probe. **(d)** Dimensions of the fiber bundle. MAP, maximum amplitude projection; PA; photoacoustic; Sync., synchronization; Trig., trigger; US, ultrasound.

WBHUS/PA imaging system and characterization

Fig. 1 describes a schematic of the WBHUS/PA dual-modal imaging system, integrating a handheld 3D scanner. Both the harmonic US and PA imaging can achieve

20-Hz 2D frame rate over 38 mm × 45 mm. For 3D imaging, the system takes 10 seconds, the time for a single breath-hold, to acquire two volumetric datasets over 38 mm × 45 mm × 50 mm. The fast imaging speed can effectively reduce the diagnosis time and enable dynamic physiological monitoring.

To accurately align the US and PA images, we develop a calibration method without using extra hardware (Materials and methods). Dual-modal imaging of a segment of tungsten wire (20-μm diameter) is shown in Supplementary Fig. S2c. Without calibration, we can observe misalignment between the US and PA images, and the PA image shows strong artifacts. With calibration, the misalignment between the US and PA images is corrected, and the PA image quality is enhanced due to accurate alignment of the radio-frequency acoustic signals.

Fig. 2a shows two representative groups of transmitted acoustic field maps in one wide-beam harmonic imaging cycle. Multi-elements are combined to extend the covering region in a single transmission event. To acquire a 2D harmonic image, we scan 96 steps with a 200-μs step interval. In comparison, conventional FIHUS scan 256 steps, which is 266% slower than WBHUS in scanning. In addition, WBHUS has a smaller data size and thus is more computationally efficient than FIHUS.

Fig. 2b shows the spatial resolutions of US and PA imaging measured in deionized water. Fig. 2c and 2d compare the cross-sectional images of the human finger joint using WBHUS and FIHUS. Compared with FIHUS, WBHUS shows nearly the same imaging quality but uses much less time. The CNR and SNR are calculated from different vessels. The vessels show hypoechoic in the US image. A background region is selected from the upper epidermis region. The two methods show no significant difference in SNR and CNR (Supplementary Fig. S4).

Fig. 2e-2h show the detailed features in the WBHUS, FIUS, and PWUS. In all three figures, the pencil lead can be seen at 17.2-mm deep in the chicken breast tissue. The WBHUS image shows more details (R1 in Fig. 2h) and sharper boundary (R1' in Fig. 2h and Supplementary Fig. S5c) than the other two.

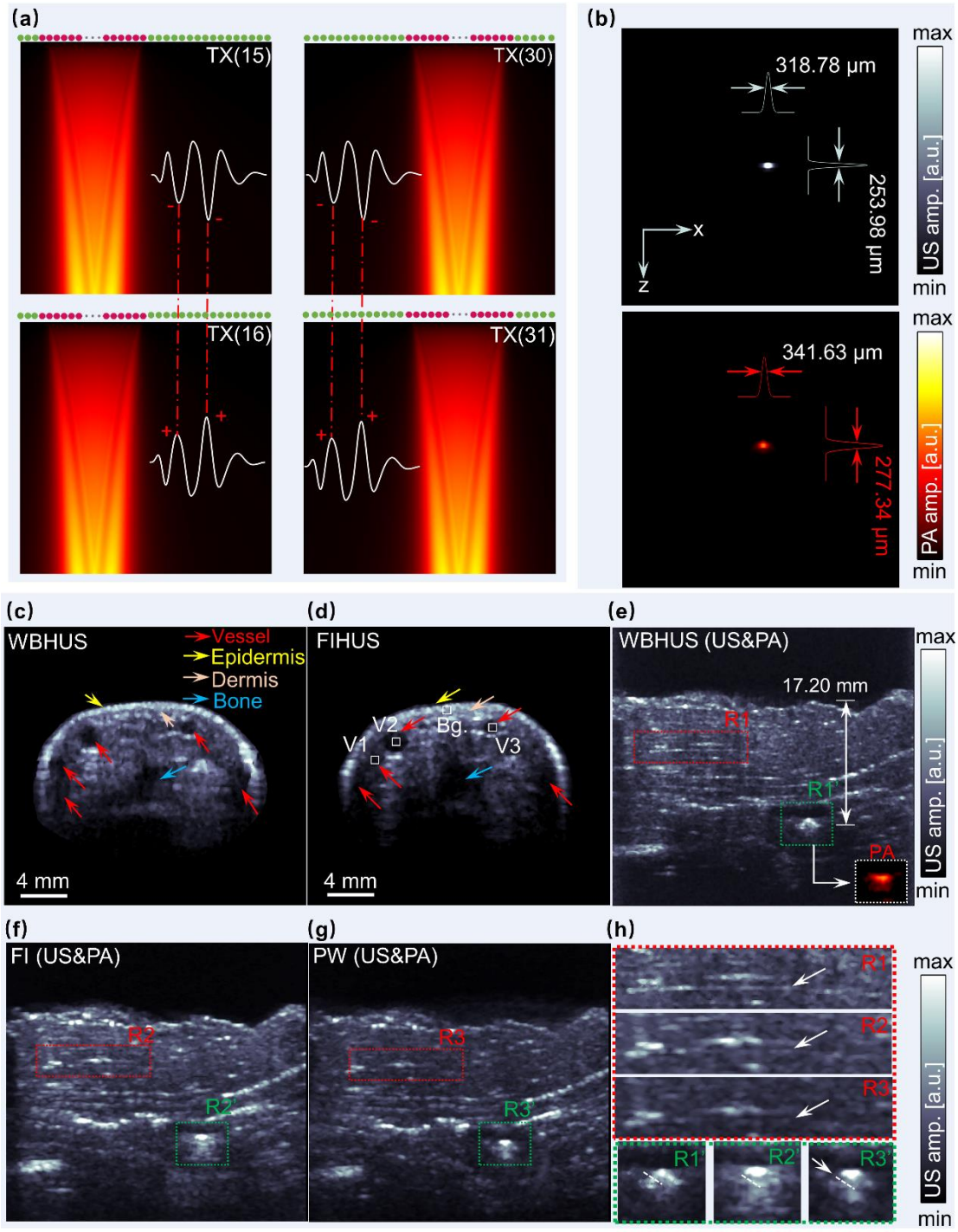

Fig. 2. Characterization of the WBHUS/PA system. **(a)** Two representative groups (pulse inversed in each group) of transmission acoustic field maps at different scanning times. The red and green spots represent the active and inactive elements, respectively. **(b)** Spatial resolutions of US and PA imaging measured in deionized water. **(c)** Cross-sectional image of an adult finger joint acquired using the WBHUS. **(d)** Cross-sectional image of an adult finger joint acquired using the FIHUS method. The image quality comparison among the WBHUS **(e)**, FI **(f),** and PW **(g)** methods via

imaging a pencil lead embedded into a chicken breast. **(h)** Close-up view of regions in the **(e)**, **(f)**, and **(g)**. The arrows show the improvement using WBHUS. amp., amplitude; Bg., background; V1, V2, and V3 denote different vascular cross-section positions for SNR and CNR calculations.

Real-time visualization of dye injection

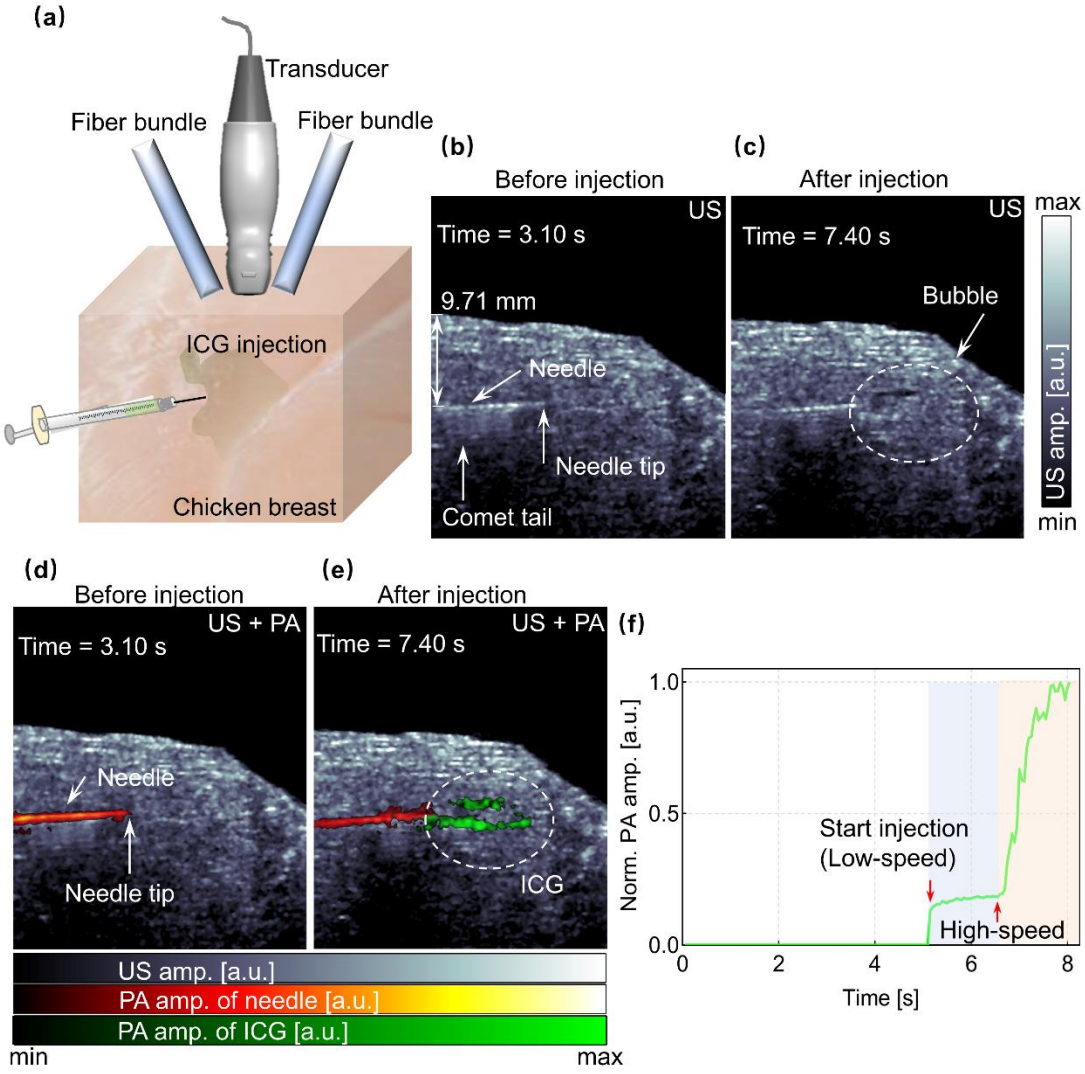

Fig.3. Dual-modal imaging for needles guidance with ICG solution injection into the chicken breast. **(a)** Schematic of dual-modal imaging and needle injection. The US image for needle guidance before injection **(b)** and after injection **(c)**. The overlaid US/PA image for needle guidance before injection **(d)** and after injection **(e)**. **(f)** The ICG concentration changes as a function of time before and after needle injection. The dashed-line circle defines the region in **(e)** for PA concentration change quantization of ICG solution.

To demonstrate the video-rate imaging speed and potential clinical applications, an

imaging-guided interventional procedure was implemented in biological tissue. The detailed operation procedure is described in Materials and methods. Fig. 3a shows a schematic of the imaging guidance for needle injection. The harmonic US images can track the needle tip in real-time (Fig. 3b) and provide its accurate position in the tissue. However, artifacts generated from multi-reflection or bubbles (Fig. 3c) are still discernible[33]. In contrast, the overlaid US/PA image provides a superior image contrast. In the PA image, both the needle tip and the ICG release process can be well visualized (Fig. 3d and Fig. 3e). We can also observe the dynamic changes when adjusting the ICG injection speed (Fig. 3f). Supplementary Movie 1 shows the whole dynamic process.

Small animal imaging and hemodynamics analysis

Animal imaging is important for pre-clinical research. Here, we demonstrate dual-modal harmonic US and PA imaging of mice. The mouse model and experimental procedures are described in Materials and methods. 1064 nm was used for PA excitation because of relatively low scattering and high laser power. Via 1D mechanical scanning, we non-invasively acquired the vascular network (Fig. 4c) ranging from the abdominal cavity to the thoracic cavity (Region R3 in Fig. 4a). The total scanning time is 8.4 seconds. The detailed structures, such as the liver lobe, the processus xiphoideus (PX), thoracic aorta, and other vessels, can be revealed from the image (maximum amplitude projection, or MAP). Fig. 4b and Fig. 4d show the co-registered US and PA images from the selected cross-sectional slice near the liver (Line R1 in Fig. 4a) and the heart (Line R2 in Fig. 4a). The harmonic US image shows a clear anatomical structure, such as the spinal cord, liver region (Fig. 4b), atrioventricular valve, and thoracic aorta (Fig. 4d), which provides a high-resolution reference for the PA features.

Aortic-related diseases are life-threatening and need early diagnosis and monitoring. To analyze the hemodynamics in the aorta, we continuously monitored the cross-section of the aorta (R2 in Fig. 4a) for 10 seconds. The pulsation of the thoracic aorta causes amplitude and displacement changes in the harmonic US and PA images. Via analyzing the PA amplitude, the pulsation is tracked and segmented automatically (Materials and

methods). We quantify the aorta regions using a circle with an 8-pixel radius (green solid circle in Fig. 4e). Representative PA images in one heartbeat cycle (0.3~0.4s) are shown in Fig. 4e. We observe strong periodic pulsation in the aorta amplitude. We also record the signal position changes along the white solid line in Fig. 4d. Both changes are temporally correlated with the heartbeat and therefore can reflect cardiovascular dynamics. Via Fourier analysis of the displacement (Fig. 4g) and amplitude (Fig. 4i), the heartbeat frequency can be determined as ~2.88 Hz. Because of the high sensitivity, we can even detect the second (5.75 Hz) and third harmonics (8.62 Hz) of the heartbeat. The dynamic images of the aorta are shown in Supplementary Movie 2 and Movie 3.

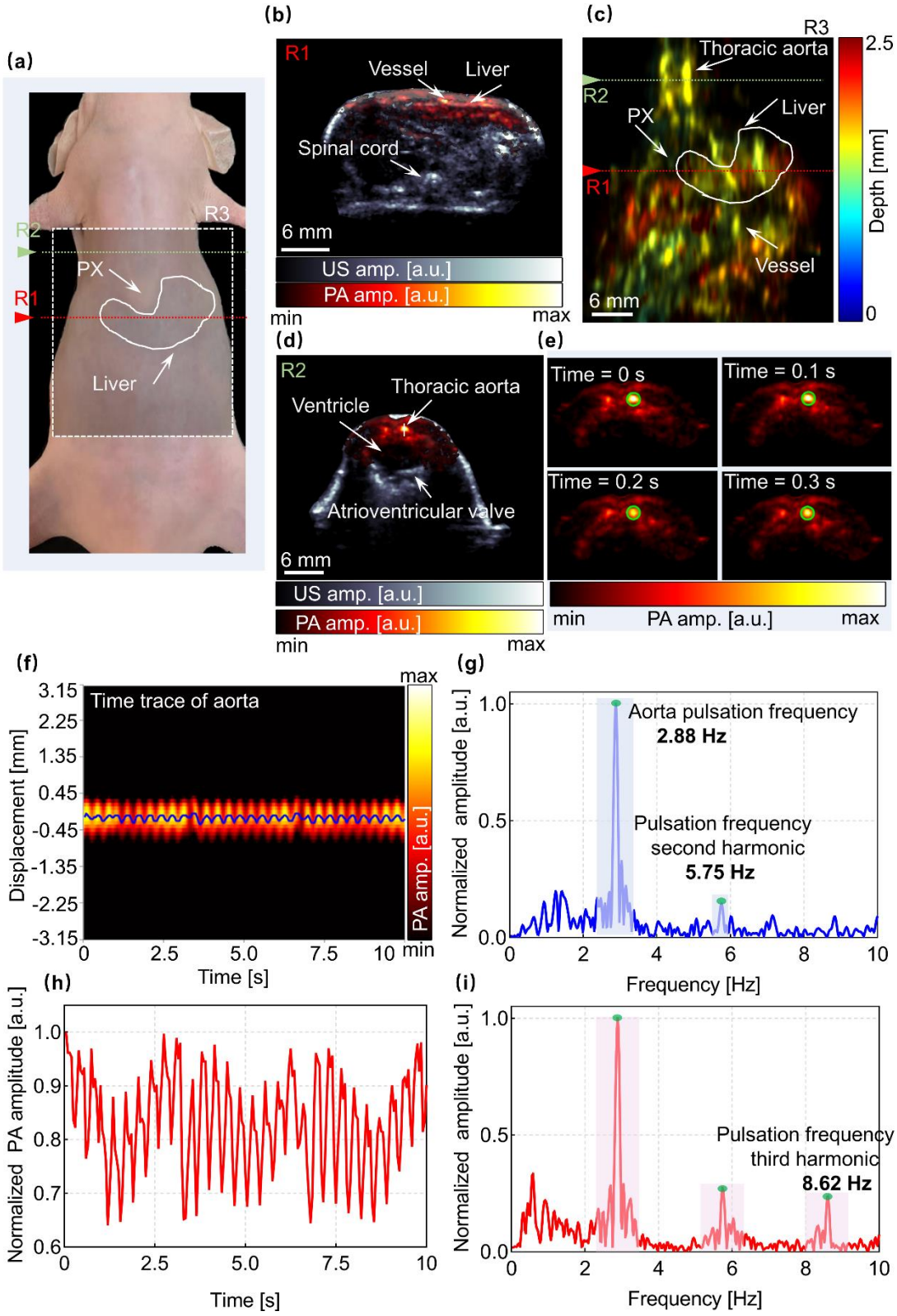

Fig.4. Dual-modal harmonic US and PA imaging of mice. **(a)** Photograph of the region of imaging. **(b)** Overlaid harmonic US and PA images at the cross-section of the liver (indicated by line R1 in **(a)**). **(c)** Top-view maximum amplitude projected PA image of R3 region in (**a**). **(d)** Overlaid harmonic US and PA images at the cross-section of the heart (indicated by line R2 in **(a)**). **(e)** Four

snapshot PA images of the thoracic aorta in about one heartbeat cycle (0.3 - 0.4 seconds). **(f)** Aortic displacement on the vertical line in **(d).** Peak amplitude positions are plotted as blue solid lines. **(g)** Fourier transforms of displacement which shows the fundamental and second-harmonic frequencies. **(h)** PA amplitude of the tracked aorta in **(e)**. **(i)** Fourier transforms of the aortic amplitude which shows the fundamental, second- and third-harmonic frequencies. PX, processus xiphoideus.

Human finger and forearm imaging

For human imaging, harmonic US imaging using a clinical-grade low-frequency linear array transducer can improve spatial resolution and reduce clutters. Integration of harmonic US and PA imaging is more suitable for human imaging but has not been thoroughly explored. Here, we demonstrate the WBHUS/PA imaging system on human finger and forearm imaging. The experimental details are described in Materials and methods. Taking advantage of the 3D imaging ability, we acquired co-registered US/PA volumetric datasets of the finger (38 mm × 45mm × 50 mm, 10 seconds) and forearm (38 mm × 45 mm × 60 mm, 12 seconds). The time for acquire one dataset is within a single breath-hold time, which effectively reduces the motion artifacts in diagnosis.

Fig. 5a and Fig. 5d show representative co-registered harmonic US/PA images. We show tomographic images in the coronal, sagittal, and transverse planes. The co-registered images exhibit rich structures, such as the skin, blood vessels, bones, and muscle-tendons. These structures are convenient for clinicians to ascertain lesion locations by retrospective inspection, for example, in the diagnosis of chronic arthritis, atherosclerosis, type 2 diabetes[34].

We extract and map the vascular network of the finger (R1 in Fig. 5a) and forearm (R2 in Fig. 5d). Because the US and PA signals from the epidermis are much stronger than that from the deep tissue, as shown in Fig. 5b and Fig. 5e, we use the co-registered US/PA image to separate the skin from others (Materials and methods). The separated images without skin are shown in Fig. 5b and Fig. 5e. The improvement is highlighted by rectangles. To further enhance the major vascular features, a vessel enhancement algorithm is applied to the images after skin removal. The results are shown with depth-encoded pseudo-color in Fig. 5b and Fig. 5e. We use the time-lapsed volumetric datasets

to plot the 3D images (Fig. 5c, Fig. 5f, Materials and methods). After the removal of the skin signals, the deep features become more visible. A comparison between the 3D PA images with and without skin removal can be seen in Supplementary Fig. 6.

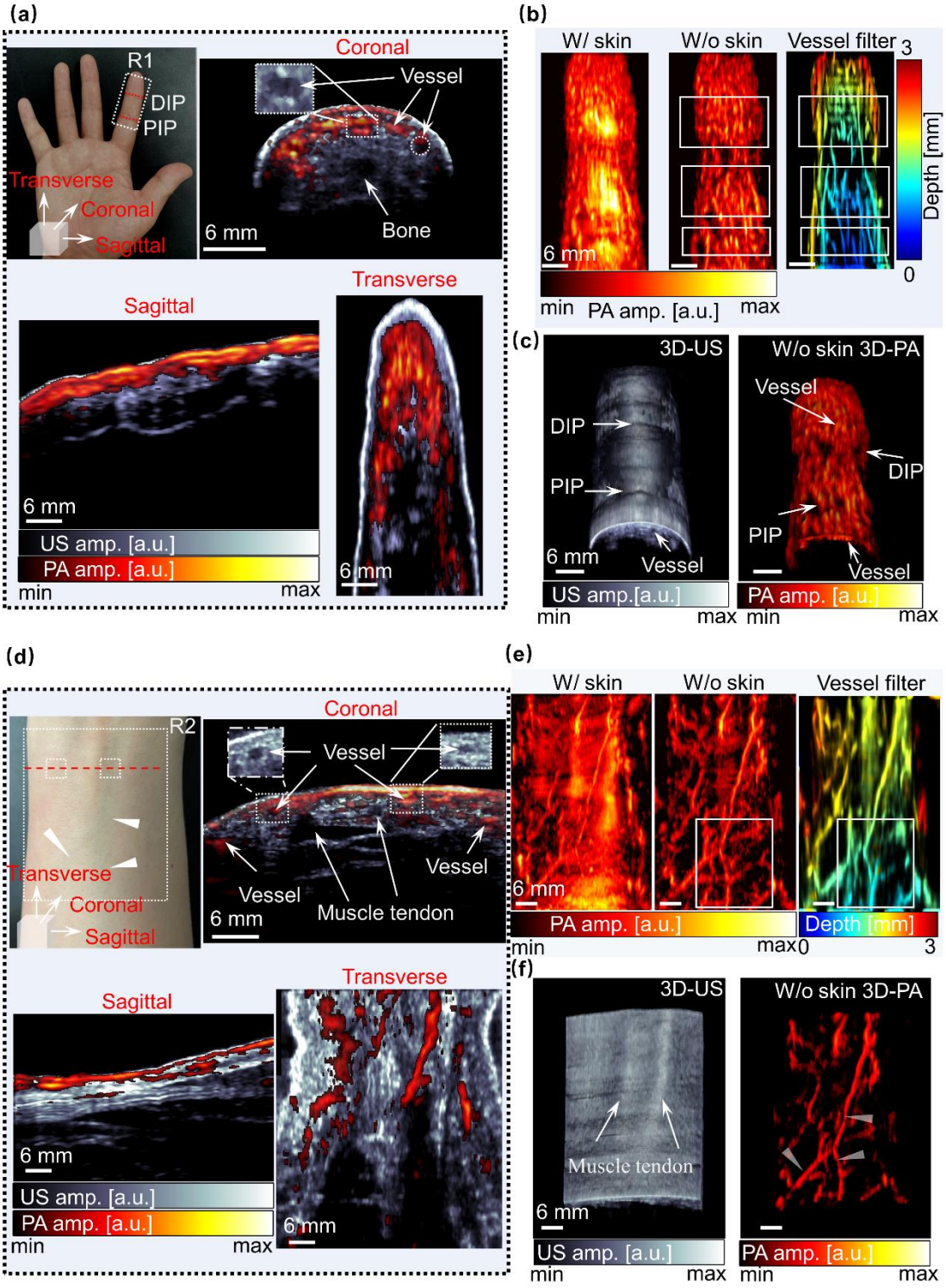

Fig.5. Dual-modal harmonic US and PA imaging of the human finger and forearm. **(a)** Photography of the finger and representative co-registered harmonic US and PA images in the

coronal, sagittal, and transverse planes. **(b)** Projected PA images of the finger with and without the skin, and vessel-enhanced PA image. The rectangles highlight the image quality enhancement. **(c)** A 3D US image and the corresponding skin-removed 3D PA image of the finger. **(d)** Photography and representative co-registered US/PA images of the forearm in the coronal, sagittal, and transverse planes. **(e)** Projected PA images of the forearm with and without the skin, and with vessel enhancement. The rectangle highlights the image quality enhancement. **(f)** A 3D US image and the corresponding skin-removed 3D PA image of the forearm. DIP, distal interphalangeal joints; PIP, proximal interphalangeal; W, with; W/o, without.

Localization and dynamic analysis of the human radial artery

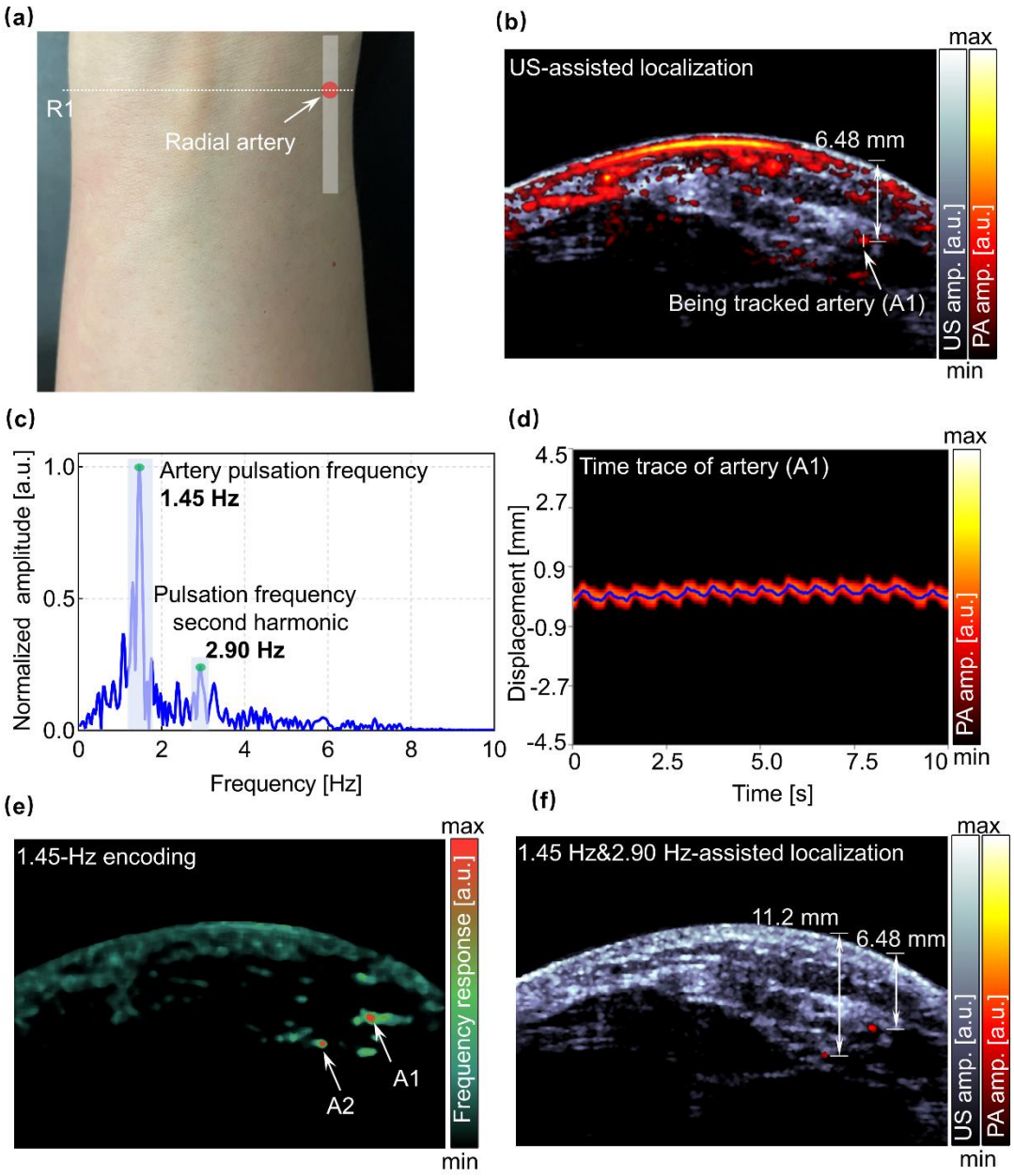

Fig.6. Dynamic analysis and localization of the radial arteries. **(a)** Photography of the human forearm for arterial pulsation measurement. **(b)** Overlaid US/PA images. An artery at 6.48-mm deep is tracked for pulsation measurement. **(c)** Fourier transform of the average arterial signal on the line profile in **(d)**. The fundamental and second-harmonic frequencies of the heartbeat are detectable. **(d)** The displacement versus time on the line profile in **(b)** and the time-trace is extracted with a blue solid line. **(e)** Pseudo-color PA image encoded with the 1.45-Hz heartbeat frequency. **(f)** Overlaid US and segmented arterial PA image.

Using video-rate harmonic US and PA imaging, we continuously monitored a cross-

section area in the forearm, as highlighted by R1 in Fig. 6a. We used 18.4-mJ/cm^2 skin-surface fluence (1064 nm) for deep imaging. According to the harmonic US and the pulsation-encoded PA imaging, we can locate the radial arteries (A1 in Fig. 6b). We recorded the arterial position (Fig. 6d)) change along the white solid line in Fig. 6b (Materials and methods). Via Fourier transformation, we can determine the fundamental and harmonic frequencies of the heartbeat from the major radial artery (Fig. 6c). We analyze the temporal frequency of each pixel in the PA images. As shown in Fig. 6e, the magnitude of the heartbeat frequency is used to encode the blood vessels with pseudo color (Supplementary Fig. S7). In such a way, the artery with strong pulsation can be separated from others. We overlay the segmented PA image on the harmonic US image. We can observe one more artery with strong pulsation (Fig. 6f and Supplementary Movie 4).

4. Discussions

We develop a dual-modal system integrating wide-beam harmonic US and single-shot PA imaging using a clinical linear-array transducer. The system can achieve video-rate imaging speed (only limited by the laser pulse repetition rate) and high imaging quality (2D and 3D).

In clinics, linear-array transducers are more widely used than other complex-shaped transducers. However, because of limited bandwidth, partial detection coverage and inadequate spatial sampling rate, PA imaging using a clinical linear-array transducer usually suffers from limited view and degraded imaging quality. Here, we address this problem via using high-speed harmonic US imaging. The harmonic US imaging provides high-resolution anatomical references for PA imaging and can therefore offer complementary contrasts. Without using dense-element and high-frequency transducers, our method provides a low-cost and high-quality dual-model US and PA imaging technique.

We demonstrate the imaging system on phantom, small animal, and human imaging. Taking advantage of high imaging speed, we can visualize interventional

procedures and observe dye injection in real-time. We also conducted longitudinal monitoring of hemodynamics of the mouse thoracic aorta and the human radial artery. The quantitative results present promising in cardiovascular-related applications. Improved quality in harmonic US and co-registered PA imaging offers clear 2D/3D anatomical structures and vascular networks in deep tissue. The dual-modal harmonic US and PA imaging system can be potentially used in many clinical applications, such as the diagnosis of dermatology, synovial arthritis, and chronic coronary artery.

In the future clinical translation, we need to be aware of or further address some limitations. Firstly, the harmonic US image is mainly used to provide an anatomical reference and to reduce skin signal interference in deep PA images. The partial detection view has not been fully addressed in PA imaging. Secondly, in the WBHUS imaging, only partial transmitted energy can be converted into harmonic signals, leading to reduced sensitivity. Because of increased attenuation in the high-frequency ultrasound, the penetration of the harmonic US imaging is less than conventional US imaging. Thirdly, limited by the wavelength and pulse repetition rate of the current laser, functional imaging of oxygen saturation has not been implemented, which can be addressed using multiple lasers for PA excitation in the future [17][29].

5. Reference

[1] M. Tanter and M. Fink, "Ultrafast imaging in biomedical ultrasound," *IEEE Trans. Ultrason. Ferroelectr. Freq. Control*, vol. 61, no. 1, pp. 102–119, 2014.

[2] L. V. Wang and S. Hu, "Photoacoustic tomography: In vivo imaging from organelles to organs," *Science*, vol. 335, no. 6075. American Association for the Advancement of Science, pp. 1458–1462, 23-Mar-2012.

[3] L. V. Wang and J. Yao, "A practical guide to photoacoustic tomography in the life sciences," *Nature Methods*, vol. 13, no. 8. Nature Publishing Group, pp. 627–638, 28-Jul-2016.

[4] C. Liu, J. Chen, Y. Zhang, J. Zhu, and L. Wang, "Five-wavelength optical-resolution photoacoustic microscopy of blood and lymphatic vessels," *Adv.*

Photonics, vol. 3, no. 01, p. 016002, Jan. 2021.

[5] D. Li, C. Liu, Y. Yang, L. Wang, and Y. Shen, "Micro-rocket robot with all-optic actuating and tracking in blood," *Light Sci. Appl.*, vol. 9, no. 1, pp. 2047–7538, Dec. 2020.

[6] J. Chen, Y. Zhang, X. Li, J. Zhu, D. Li, S. Li, C.-S. Lee, and L. Wang, "Confocal visible/NIR photoacoustic microscopy of tumors with structural, functional, and nanoprobe contrasts," *Photonics Res.*, vol. 8, no. 12, p. 1875, Dec. 2020.

[7] S. Li, Q. Deng, Y. Zhang, X. Li, G. Wen, X. Cui, Y. Wan, Y. Huang, J. Chen, Z. Liu, L. Wang, and C. Lee, "Rational Design of Conjugated Small Molecules for Superior Photothermal Theranostics in the NIR-II Biowindow," *Adv. Mater.*, vol. 32, no. 33, p. 2001146, Aug. 2020.

[8] M. Zha, X. Lin, J. Ni, Y. Li, Y. Zhang, X. Zhang, L. Wang, and K. Li, "An Ester-Substituted Semiconducting Polymer with Efficient Nonradiative Decay Enhances NIR-II Photoacoustic Performance for Monitoring of Tumor Growth," *Angew. Chemie Int. Ed.*, vol. 59, no. 51, pp. 23268–23276, Dec. 2020.

[9] G. Wen, X. Li, Y. Zhang, X. Han, X. Xu, C. Liu, K. W. Y. Chan, C. S. Lee, C. Yin, L. Bian, and L. Wang, "Effective Phototheranostics of Brain Tumor Assisted by Near-Infrared-II Light-Responsive Semiconducting Polymer Nanoparticles," *ACS Appl. Mater. Interfaces*, vol. 12, no. 30, pp. 33492–33499, Jul. 2020.

[10] C. Yin, X. Li, G. Wen, B. Yang, Y. Zhang, X. Chen, P. Zhao, S. Li, R. Li, L. Wang, C. S. Lee, and L. Bian, "Organic semiconducting polymer amphiphile for near-infrared-II light-triggered phototheranostics," *Biomaterials*, vol. 232, p. 119684, Feb. 2020.

[11] K. P. Kubelick and S. Y. Emelianov, "In vivo photoacoustic guidance of stem cell injection and delivery for regenerative spinal cord therapies," *Neurophotonics*, vol. 7, no. 03, p. 1, Jul. 2020.

[12] A. Wiacek and M. A. Lediju Bell, "Photoacoustic-guided surgery from head to

toe [Invited]," *Biomed. Opt. Express*, vol. 12, no. 4, 2021.

[13] T. Wei, J. Liu, D. Li, S. Chen, Y. Zhang, J. Li, L. Fan, Z. Guan, C. Lo, L. Wang, K. Man, and D. Sun, "Development of Magnet-Driven and Image-Guided Degradable Microrobots for the Precise Delivery of Engineered Stem Cells for Cancer Therapy," *Small*, vol. 16, no. 41, p. 1906908, Oct. 2020.

[14] E.-Y. Park, S. Park, H. Lee, M. Kang, C. Kim, and J. Kim, "Simultaneous Dual-Modal Multispectral Photoacoustic and Ultrasound Macroscopy for Three-Dimensional Whole-Body Imaging of Small Animals," *Photonics*, vol. 8, no. 1, p. 13, Jan. 2021.

[15] S. Choi, J. Y. Kim, H. G. Lim, J. W. Baik, H. H. Kim, and C. Kim, "Versatile Single-Element Ultrasound Imaging Platform using a Water-Proofed MEMS Scanner for Animals and Humans," *Sci. Rep.*, vol. 10, no. 1, pp. 1–9, Dec. 2020.

[16] J. Kim, S. Park, Y. Jung, S. Chang, J. Park, Y. Zhang, J. F. Lovell, and C. Kim, "Programmable Real-time Clinical Photoacoustic and Ultrasound Imaging System," *Sci. Rep.*, vol. 6, no. 1, pp. 1–11, Oct. 2016.

[17] G. S. Jeng, M. L. Li, M. W. Kim, S. J. Yoon, J. J. Pitre, D. S. Li, I. Pelivanov, and M. O'Donnell, "Real-time interleaved spectroscopic photoacoustic and ultrasound (PAUS) scanning with simultaneous fluence compensation and motion correction," *Nat. Commun.*, vol. 12, no. 1, pp. 1–12, Dec. 2021.

[18] A. Garcia-Uribe, T. N. Erpelding, A. Krumholz, H. Ke, K. Maslov, C. Appleton, J. A. Margenthaler, and L. V. Wang, "Dual-Modality photoacoustic and ultrasound imaging system for noninvasive sentinel lymph node detection in patients with breast cancer," *Sci. Rep.*, vol. 5, no. 1, pp. 1–8, Oct. 2015.

[19] A. A. Oraevsky, B. Clingman, J. Zalev, A. T. Stavros, W. T. Yang, and J. R. Parikh, "Clinical optoacoustic imaging combined with ultrasound for coregistered functional and anatomical mapping of breast tumors," *Photoacoustics*, vol. 12, pp. 30–45, Dec. 2018.

[20] K. Joseph Francis, Y. E. Boink, M. Dantuma, M. K. Ajith Singh, S. Manohar, and W. Steenbergen, "Tomographic imaging with an ultrasound and LED-

based photoacoustic system," *Biomed. Opt. Express*, vol. 11, no. 4, p. 2152, Apr. 2020.

[21] E. Merčep, G. Jeng, S. Morscher, P. C. Li, and D. Razansky, "Hybrid optoacoustic tomography and pulse-echo ultrasonography using concave arrays," *IEEE Trans. Ultrason. Ferroelectr. Freq. Control*, vol. 62, no. 9, pp. 1651–1661, Sep. 2015.

[22] Y. Zhang and L. Wang, "Video-Rate Ring-Array Ultrasound and Photoacoustic Tomography," *IEEE Trans. Med. Imaging*, vol. 39, no. 12, pp. 4369–4375, Dec. 2020.

[23] E. Merčep, J. L. Herraiz, X. L. Deán-Ben, and D. Razansky, "Transmission–reflection optoacoustic ultrasound (TROPUS) computed tomography of small animals," *Light Sci. Appl.*, vol. 8, no. 1, pp. 2047–7538, Dec. 2019.

[24] M. Nishiyama, T. Namita, K. Kondo, M. Yamakawa, and T. Shiina, "Ring-array photoacoustic tomography for imaging human finger vasculature," *J. Biomed. Opt.*, vol. 24, no. 09, p. 1, Sep. 2019.

[25] A. Ron, S. K. Kalva, V. Periyasamy, X. L. Deán-Ben, and D. Razansky, "Flash Scanning Volumetric Optoacoustic Tomography for High Resolution Whole-Body Tracking of Nanoagent Kinetics and Biodistribution," *Laser Photonics Rev.*, vol. 15, no. 3, Mar. 2021.

[26] E. Mercep, X. L. Dean-Ben, and D. Razansky, "Combined Pulse-Echo Ultrasound and Multispectral Optoacoustic Tomography with a Multi-Segment Detector Array," *IEEE Trans. Med. Imaging*, vol. 36, no. 10, pp. 2129–2137, Oct. 2017.

[27] Y. Gao, A. Tannenbaum, H. Chen, M. Torres, E. Yoshida, X. Yang, Y. Wang, W. Curran, and T. Liu, "Automated skin segmentation in ultrasonic evaluation of skin toxicity in breast cancer radiotherapy," *Ultrasound Med. Biol.*, vol. 39, no. 11, pp. 2166–2175, 2013.

[28] J. Kim, J. Y. Kim, S. Jeon, J. W. Baik, S. H. Cho, and C. Kim, "Super-resolution localization photoacoustic microscopy using intrinsic red blood cells as contrast absorbers," *Light Sci. Appl.*, vol. 8, no. 1, pp. 2047–7538, Dec.

2019.

[29] L. Li, L. Zhu, C. Ma, L. Lin, J. Yao, L. Wang, K. Maslov, R. Zhang, W. Chen, J. Shi, and L. V. Wang, “Single-impulse panoramic photoacoustic computed tomography of small-animal whole-body dynamics at high spatiotemporal resolution,” *Nat. Biomed. Eng.*, vol. 1, no. 5, p. 71, May 2017.

[30] ZUIDERVELD and K., “Contrast Limited Adaptive Histogram Equalization,” *Graph. Gems*, pp. 474–485, 1994.

[31] S. Yousefi, J. Qin, Z. Zhi, and R. K. Wang, “Uniform enhancement of optical micro-angiography images using Rayleigh contrast-limited adaptive histogram equalization.,” *Quant. Imaging Med. Surg.*, vol. 3, no. 1, pp. 5–17, 2013.

[32] M. Xu and L. V. Wang, “Photoacoustic imaging in biomedicine,” *Review of Scientific Instruments*, vol. 77, no. 4. American Institute of PhysicsAIP, p. 41101, 17-Apr-2006.

[33] J. Su, A. Karpiouk, B. Wang, and S. Emelianov, “Photoacoustic imaging of clinical metal needles in tissue,” *J. Biomed. Opt.*, vol. 15, no. 2, p. 021309, 2010.

[34] A. Berezhnoi, J. Aguirre, B. Hindelang, N. Garzorz-Stark, M. Omar, U. Darsow, K. Eyerich, and V. Ntziachristos, “Optical features of human skin revealed by optoacoustic mesoscopy in the visible and short-wave infrared regions,” *Opt. Lett.*, vol. 44, no. 17, p. 4119, Sep. 2019.